Abundant fluids in southern Kumano Basin linked to fluid source and slow earthquakes at plate boundary in Nankai Trough

Authors: Xin Liu[1,2], Ayako Nakanishi[1], Gou Fujie[1], Takashi Tonegawa[1], Yasuyuki Nakamura[1], Koichiro Obana[1] and Shuichi Kodaira[1]

Affiliations:

[1] JAMSTEC

[2] Department of Earth Sciences, University of Hong Kong

*Correspondence to: liuxine@hku.hk

Abstract

The Nankai Trough is a major subduction zone in SW Japan capable of generating the next M7 or larger earthquake off Kii Peninsula. In addition to earthquakes characterized by sharp P and S arrivals, there are numerous slow earthquakes without clear P phases at the subducting plate boundary corresponding to transient slips that are related to fluids at the plate boundary and high pore pressure. In this study, we perform ambient noise differential adjoint tomography to derive the S-wave velocity model beneath a linear Ocean Bottom Seismometer (OBS) array, which was previously difficult based on airgun active source study. We discover that S-wave velocities in the southern (seaward) Kumano Basin are significantly lower than in the northern (landward) Kumano Basin, suggesting weak upper plate and abundant fluids in the southern Kumano Basin. The fluid-rich southern Kumano Basin lies above a weak interplate coupling zone with shallow slow earthquakes and pressurized fluids due to plate interface dehydration. Conversely, the northern Kumano Basin overlies a strong interplate coupling zone with few slow earthquakes, suggesting fluid migration from the weak-coupling interface to the forearc basin above.

Significance statement

Extracting S wave velocity is difficult using traditional active-source marine datasets as the airguns at sea surface do not generate S-waves. Previous P-wave tomography in subduction zones shows small lateral variations around 10%. This paper extends a new method for S wave tomography in marine subduction zone. The ambient noise differential adjoint tomography reveals more than 50% reduction in S-wave velocity in the southern Kumano Basin, validated by its remarkable correspondence with the MCS seismic reflection profile of the sedimentary basin. Low velocity in southern Kumano basin indicates abundant fluids, overlapping with slow earthquakes that are rare in the northern Kumano Basin where fluids are sparse. This finding suggests fluids migration from plate boundary to the overlaying southern Kumano Basin.

MAIN TEXT

Introduction

The Nankai Trough is a major subduction zone south of Japan's Honshu Island. It is formed by the Philippine Sea Plate (PSP) subducting beneath the Eurasian Plate (Figure 1). The recurrence interval of large earthquakes greater than magnitude 8 is about 100-200 years in the Nankai Trough (1–4). The convergence rate ranges from ~4.1-6.5 cm/year due to the three-dimensional shape of the subducting PSP and the curved deformation front (5, 6). This large convergence rate suggests that the megathrust earthquakes happen repeatedly at the seismogenic zone due to accumulation of strain energy (7). Constraining the seismogenic depth ranges along the Nankai Trough is therefore crucial for predicting the strong seafloor ground shaking, which is a main factor in estimating the size of potential tsunamis.

The 1944 Tonankai earthquake, with magnitude 8.1, caused strong ground shaking and a tsunami in southeastern coast of central Japan (3), resulting in 1250 deaths. Splay faults branching off from the plate interface fault are found at ~10 km depth in the Tonankai area off the Kii Peninsula (8, 9). These splay faults could have slipped during the earthquake to reach the seafloor, which potentially increased the tsunami wave amplitude (10). The 1946 Nankaido earthquake, with a similar magnitude (1–3), resulted in 1362 casualties and significant damage to many homes. It also generated a tsunami with 5–6-meter waves. Seismologists deduced that a subducted seamount at a depth of 10 km might have formed a barrier allowing the earthquake rupture to propagate along the plate interface of the Nankai subduction zone (4).

The Kumano Basin is a forearc basin located in the Nankai subduction zone, where the Philippine Sea plate is subducting beneath the Eurasia plate. The ocean floor of the basin is situated at a water depth of approximately 2 km, overlying a thick sequence (up to 2 km) of sediments. The bottom of the basin is part of the accretionary prism under compression and deformation due to the subduction at the convergent plate boundary. As a result, cracks and small faults are formed, creating passages ways for fluid migration beneath and within the basin (5, 11).

The shallow slow earthquakes in Nankai Trough are located in spatially limited regions (Figure 1) and they occur in the weakly coupled zone above the stably locked plate interface (12, 13). There are various types of shallow slow earthquakes off Kii Peninsula in Nankai Trough: e.g., very low frequency earthquakes (VLFEs) (14, 15, 12, 16–19) and tremors (20–22). The VLFEs are typically detected in 0.01-0.1 Hz frequency band, while the tremors are in 1-10 Hz band. The spatial distributions of VLFEs and tremors partially overlap, and they cover a large region from southern Kumano Basin to the Trench axis (Figure 1). The overlapping spatial pattern of VLFEs and tremors suggests a broadband slow earthquake phenomenon that the low- and high-frequency slow earthquakes are common components of a broadband slow slip process (23). Moreover, shallow slow slip events (SSEs) have been detected as the pore-pressure changes associated with the occurrence of these events observed by borehole measurements (24). Nakano et al. (2018) (12) suggested that shallow SSEs and VLFEs result from a common slip process on the same fault plane, as indicated by the pore-pressure-change time series.

In this paper, we apply the ambient noise differential adjoint tomography to derive the shear (S) wave velocity structure in the top 5 km depth beneath the KI03 linear OBS array (Figure 1), which consists of 30 OBS seismometers with four components including a hydrophone. This new differential adjoint tomography method reduces the bias caused by uneven noise source distributions by suppressing the sensitivity to noise sources. The KI03 array crosses the western portion of the Kumano Basin and the tomography results reveal thick water-bearing sediments corresponding to low S-wave velocity in the southern part of the basin, which coincides with the northwestern boundary of shallow slow earthquakes. Additionally, slow S-wave velocity also appear at the trench sediments above the subducting oceanic plate, suggesting water being carried to depths along the subducting plate interface.

Results

We use ambient noise correlations to extract Love wave phases from the transverse components of the array and perform phase velocity tomography using differential-time measurements, which reduces the sensitivity to noise sources (25, 26). We obtain the initial S-wave velocity model by converting the phase velocity tomography to S-wave velocity structure (Figure S3) beneath each horizontal location using the propagator matrix approach with flat-layer assumption (27). Then we iteratively update the S wave velocity model using ambient noise differential adjoint tomography (26).

The resulting S-wave velocity model (Figure 2a) reveals significantly low S-wave velocity in the southwestern part of the Kumano Basin and the incoming sediments above the subducting oceanic crust of the Philippine Sea Plate. Specifically, in the southwestern portion of the Kumano Basin beneath the KI03 array (for X between 65-85 km), the S-wave velocities are low, ranging between 0.2-0.5 km/s in the top 3 km depth, forming a distinctive bowl-shaped structure. For comparison, this bowl-shaped structure corresponds to approximately 40-60% velocity reduction with respect to the surrounding rocks. Considering that the P wave velocity are greater than 1.5 km/s in the top 3 km depth, the Vp/Vs ratio is between 3-7, which cannot be explained by anisotropy in sedimentary layers alone (28) without considering the presence of fluids (29, 26). Additionally, the incoming sediments overlaying the subducting oceanic crust south of the deformation front exhibit S-wave velocities between 0.5-1.0 km/s, indicating a 20-50% velocity reduction relative to the surrounding rocks.

Overlaying the S-wave velocity model with the migrated seismic reflection profile from MCS (Multi-Channel Seismic) dataset (30), we find striking agreements between the low-velocity region in southwestern Kumano Basin and seismic reflectors outlining the shape and sedimentary layers of the basin (Figure 2b). In addition, the low-velocity incoming sediment (X between 20-30 km) south of the deformation front correlates with the sedimentary layer reflections in MCS seismic profile.

The shallow structure in the top 1.5 km around splay faults shows S-wave velocity in the range of 0.6-1.0 km/s, which is slow compared with its surrounding regions. But the low velocity around splay fault is not reliable according to the checkerboard test in Materials and methods section.

The white dashed line (Figure 2) represents the estimated depth sensitivity lower bound from ray theory and flat-layer assumptions in propagator matrix approach. For each horizontal location X (km), it is the depth where the sensitivity of 8-s Love wave drops below 10% of its peak. Because this depth lower bound is derived from flat-layer assumption and ray theory, it becomes invalid in the presence of strong lateral velocity variations. Consequently, this depth lower bound from ray theory should not apply to the adjoint tomography result showing low-velocity bowl in Kumano Basin or the incoming sediment overlaying the subducting plate. It would be more appropriate to refer to the velocity update after adjoint tomography (Methodology section).

Overlaying the Multi-Channel Seismic (MCS) profile with the S-wave velocity update (Figure 3), the sedimentary layers in southern Kumano basin are outlined by strong seismic reflectors, which correlate with up to 60% velocity reduction in the basin sediments that contains abundant fluids (26, 31). Despite the strong seismic reflectors from sedimentary layers, the northern Kumano Basin, however, only shows 5-10% shear velocity reduction, suggesting that the northern Kumano Basin does not contain as much fluid as the southern Kumano Basin.

We delineate the boundaries of major geological units combining the S-wave adjoint tomography result and the MCS seismic profile (Figures S4&5). The resulting cartoon (Figure 4) shows the three main fluid-bearing structures: southern Kumano Basin, incoming sediments overlaying the subducting oceanic plate and the rocks around the splay fault, as well as their connections with the source of fluid at the plate interface right underneath the accretionary prism. The imbricate thrust faults are the possible fluid migrating paths from plate interface to Kumano Basin. In between the stations OBS74 and OBS79, the fluid-rich southern Kumano Basin overlaps with the shallow tremors and VLFEs (Figure 1), which did not extend beyond NW of the station OBS79. The downdip limit of slow-slip events (SSEs), however, is not determined (24).

Discussion

The most notable feature of the S-wave tomography image is the bowl-shaped, fluid-rich southern Kumano Basin, which shows ~50% velocity reduction and lies between OBS74 and OBS79 within the weak plate coupling zone (Figures 1, 2, 3). Interestingly, the station OBS79, which is at the NW end of the fluid-rich southern Kumano Basin, marks the NW boundary for various types of shallow slow earthquakes, i.e., the downdip boundary of the weak plate coupling zone, suggesting a link between the fluid-rich southern Kumano basin and the source regions of shallow slow earthquakes.

The relatively slow S-wave velocity in the southern Kumano Basin and the overriding plate underneath the KI03 array suggest that the upper plate is weak around the southern Kumano Basin, which favors the occurrence of slow earthquakes and aseismic slip (32–35). The relatively fast S-wave velocity in the northern Kumano Basin suggests a more rigid upper plate, which indicates higher stress accumulation. This corresponds to fewer slow earthquakes and is located near the epicenter of the 1944 M8.1 Tonankai earthquake (Figure 1).

The spatial distribution of shallow slow earthquakes in Nankai Trough generally follow the different processes the dewatering and/or mineral dehydration along the plate interface at different depths. At shallower depth (plate interface between 0-1 km below seafloor), the dewatering process is the dominant source of fluid due to increasing geothermal temperature and compaction, which is related to the fluid-rich trench sediments and the deformation front (5, 36–38). At intermediate depths (2-7 km below seafloor), the mineral dehydration (smectite-to-illite transition) process kicks in and increases its portion as the source of fluids. At deeper depths (7-9 km below seafloor), the mineral dehydration is the main source of fluids at the plate interface (39, 40), but fluid abundance decreases dramatically due to less smectite clay mineral at deeper depths, leading to fewer shallow slow earthquakes at this depth range.

The pore fluid pressure is also related to the shallow slow earthquakes at Nankai Trough (41, 42). High pore fluid pressure is required to reduce the effective normal stress on the plate interface, which is important for the occurrence of shallow slow earthquakes.

To increase/maintain the high pore fluid pressure, the fluids at the plate interface need to be temporarily sealed (17, 42).

Previous studies find evidence that connects the water in Kumano Basin with the fluid sources at the plate interface. Geochemical studies reveal that the clay mineral dehydration is the main source of fluids at the plate interface underneath Kumano Basin (5, 43, 44). The fluid generated at the plate interface must migrate upward to the southern Kumano Basin sediments if fluid conduits exist (45). Considering the consistency between the fluid-rich basin and the slow earthquake zones (Fig 3), the conduits could be imbricate thrust faults (11, 46) branching off from the plate interface reaching the bottom of the southern Kumano Basin. These imbricate thrust faults, or fluid conduits could be temporarily sealed to maintain high pore pressure at the plate interface, reducing effective normal stress and weakening plate coupling. But the high pore fluid pressure at plate interface could open the fluid conduits periodically to help the fluids migrating upwards to the Kumano Basin (17, 42, 45).

Materials and Methods

We utilize the transverse (TT) components of KI03 linear OBS array to derive Love wave phases (Figure S1). This short-period OBS array was intended for active-source surveys. The continuous data span 53 days since Oct 2011. We first apply an automatic outlier remover to remove earthquakes and other transient signals (47, 48) from the raw noise recordings. The raw data is divided into time windows of 200s. The earthquake first arrival is marked by PhaseNet and we remove the 200s window containing the earthquake. Other transient signals can be removed by constructing the time series of the maximum envelope value in each time window and identifying the outliers that exceed 5 MAD (Median Absolute Deviation) of the maximum envelope value time series. Then one-bit normalization is carried out to flatten the noise waveform in the time domain, which is followed by noise cross correlations among all station pairs.

Subsequently, we conduct phase velocity tomography by employing differential-time measurements, which significantly reduces the impact of noise sources (25). The precise procedures of phase velocity tomography are detailed in the Supplementary Material of

Liu et al (49). To increase the reliability of the differential time data, we apply strict Signal-Noise Ratio (SNR) criteria to the travel time data used for differential time measurements that the SNR must be greater than 10 and the resulting differential time should have a standard deviation less than 10% of its value. All of the travel time uncertainties are computed using bootstrap method (50).

Our method only measures the direct surface wave packets in the observed and synthetic waveform data. For multiple scattering, scattered phases arrive after the fundamental mode Love wave packet. Therefore, scattered phases should not affect the phase dispersion measurement of the direct fundamental mode of Love wave.

The initial S-wave velocity model is based on the existing P-wave velocity model (9) from marine active-source travel-time tomography. We convert the P-wave velocity to S-wave velocity using empirical relations (51) and multiply it by 0.75 to reduce the overall S-wave velocity for initial model, which is closer to the S-wave velocity model based on ambient noise ray-theory tomography.

Conventional two-station noise interferometry is sensitivity to noise sources within the Fresnel Zone in additional to the seismic velocity structure between the two stations. For instance, the travel time on the causal part of noise cross correlation can be shifted by noise sources in the Fresnel Zone from the west bounded by hyperbola (Figure S6a), known as source-structure tradeoffs (52, 53). We introduce the 3rd station to the traditional two-station setting and compute two cross correlations (Figure S6b), such that the distance between the receivers is less than 20% of the average distance from the virtual source to the pair of receivers. As a result, the differential time is insensitive to the noise sources because the Fresnel Zones of the two station pairs mostly overlap, resulting in cancelation of source sensitivity (25).

The KI03 line is perpendicular to the coast, while the noise sources are also strongest in the coast-perpendicular direction. Additionally, the Fresnel Zone, in which the noise sources add up constructively, also aligns with the strike of the linear array. Therefore, most of the energies in the TT component cross correlation come from the Love wave sources located within the Fresnel zone close to the inline direction.

We first apply the conventional phase velocity tomography with differential-time measurements from each period using the criteria above following Liu et al (49). The phase velocity tomography image (Figure S2) also illustrates significant low-velocity structure at long periods near the southern Kumano Basin. Using the standard approach based on propagator matrix and flat-layer assumption, we invert for the S-wave velocity structure underneath each horizontal location along the linear KI03 array. This S-wave velocity model is the starting model for adjoint tomography.

For adjoint tomography, we consistently identify sets of three stations (triplet) along a line where the virtual source is significantly distanced from the two proximate receivers using the criteria above. The forward wavefield is simulated by replacing the virtual source with a point source (26). The differential-time misfit function for one triplet of stations is,

$$\chi_{ij}^{dd} = \frac{1}{2}\sum_{\omega} W(\omega)\left[\Delta t_{ij}(\omega) - \Delta t_{ij}^{obs}(\omega)\right]^2, \quad (1)$$

where $\Delta t_{ij}^{obs}(\omega)$ and $\Delta t_{ij}(\omega)$ are, respectively, observed and synthetic differential time measurements between station pairs 1-*i* and 1-*j* (Figure S6b). The virtual source is denoted as "1" for simplicity. The subscripts *i* and *j* denote the two nearby receivers. ω is the angular frequency. $W(\omega)$ is a weighting function and ω is angular frequency. In this study, the Love wave dispersion data indicate that the differential times are frequency dependent.

Taking the variation of the misfit function, we obtain the perturbation in misfit function due to perturbation in elastic moduli C and density ρ (54, 55),

$$\delta\chi_{ij}^{dd} = \int_{\Omega}\left[K_C^{dd}(\mathbf{x})\frac{\delta C}{C} + K_{\rho}^{dd}(\mathbf{x})\frac{\delta\rho}{\rho}\right]d\mathbf{x}, \quad (2)$$

where K_C and K_ρ are, respectively, differential sensitivity kernels for elastic moduli and density.

The differential sensitivity kernel for elastic moduli is (56–58, 26, 59),

$$K_C^{dd}(\mathbf{x}) = -C(\mathbf{x})\int_f \nabla\mathbf{u}(\mathbf{x},\omega)\left[\nabla\mathbf{u}_j^\dagger(\mathbf{x},\omega) - \nabla\mathbf{u}_i^\dagger(\mathbf{x},\omega)\right]d\omega, \quad (3)$$

where the $\mathbf{u}(\mathbf{x})$ and $\mathbf{u}^\dagger(\mathbf{x})$ are forward and adjoint wavefields, respectively. ω is the angular frequency.

For SH wave equation in a 2D profile along a line, the above vector wavefield $\mathbf{u}(\mathbf{x})$ simplifies to scalar displacement in the crossline direction, u_y. The differential-time sensitivity kernel for shear modulus μ is,

$$K_{\mu,ij}^{dd}(\mathbf{x}) = -\mu(\mathbf{x})\int_f \nabla u_y(\mathbf{x},\omega)\cdot\left[\nabla u_{yj}^\dagger(\mathbf{x},\omega) - \nabla u_{yi}^\dagger(\mathbf{x},\omega)\right]d\omega, \quad (4)$$

where the · represents vector inner product. The adjoint sources for the two adjoint wavefields at receivers i & j are defined in Supplementary Text S1.

In differential adjoint tomography, the sensitivity kernel in eq. (4) is essentially the gradient of misfit in eq. (1) with respect to the shear modulus for one station triplet. This gradient is directly computed from the inner product of forward and adjoint wavefields in eq. (4). Combined with an optimization algorithm based on gradient descent, the differential time misfit can be reduced iteratively.

For each virtual source, all such station triplets are identified and their combined differential-time sensitivity kernel is computed in the forward and adjoint simulations. The adjoint sources are frequency dependent (26). In addition, we sum up the sensitivity kernels for all virtual sources to compute the total sensitivity kernel (Supplmentary Text S1), which is essentially the gradient of the sum of misfit functions for all virtual sources used in the iterative adjoint tomography.

The initial evaluation of the total gradient shows significant positive sensitivity to the southern Kumano Basin for X between 70 and 90 km (Figure 5a), suggesting that the starting S-wave velocity is faster compared with reality. After 10 iterations, the resulting shear velocity update resembles the main features in the initial sensitivity kernel where the southern Kumano Basin corresponds to -30-60% shear velocity reduction (Figure 5b) compared to the starting velocity model. However, the final velocity image comprises the combined effects of multiple sensitivity kernels in 10 iterations (Figure 5c) and deviates slightly from the initial sensitivity kernel.

In addition, we implement the checkerboard test (Figure S7) for differential adjoint tomography beneath the KI03 linear array. We designed two layers of checkers with alternating +/- 10% S-wave velocity perturbations to the ray-theory tomography result (starting S velocity model for adjoint tomography). The first layer of checkers has a thickness of 2 km, and the second layer has a thickness of 3 km. The width of each checker is 5 km, which is equal to the average station spacing (Figure S7a&b). Using the same starting model for real data-based adjoint tomography, the recovered checkerboard (Figure S7c) shows reliable first and second layers for X between 65 km and 120 km, except that the bottom of the second layer is slightly smeared. The second layer for X between 20 km and 30 km can be recovered. To conclude, the differential tomography method can reliably recover the S velocity anomalies at 0-5km depths for Kumano Basin and the incoming sediments south of the deformation front. The splay fault is located at X~55 km, the checkers at which cannot be uniquely recovered due to complex superposition of checkers and shallow plate interface.

Acknowledgements: Data and materials availability: All results needed to evaluate the conclusions in the paper are present in the paper and/or the Supplementary Materials. The continuous data on KI03 OBS can be obtained from JAMSTEC seismic database site https://www.jamstec.go.jp/obsmcs_db/e/ with DOI number DOI: 10.17596/0001152. The MCS data can be obtained from the same JAMSTEC Seismic Survey Database Site http://www.jamstec.go.jp/obsmcs_db/e/survey/data_area.html?cruise=KR01-08 with DOI number doi:10.17596/0002069.

Reference

1. H. Kanamori, Mechanism of tsunami earthquakes. *Phys. Earth Planet. Inter.* **6**, 346–359 (1972).

2. M. Ando, Source mechanisms and tectonic significance of historical earthquakes along the nankai trough, Japan. *Tectonophysics* **27**, 119–140 (1975).

3. T. Furumura, T. Hayakawa, M. Nakamura, K. Koketsu, T. Baba, Development of Long-period Ground Motions from the Nankai Trough, Japan, Earthquakes: Observations and Computer Simulation of the 1944 Tonankai (Mw 8.1) and the 2004 SE Off-Kii Peninsula (Mw 7.4) Earthquakes. *Pure Appl. Geophys.* **165**, 585–607 (2008).

4. S. Kodaira, N. Takahashi, A. Nakanishi, S. Miura, Y. Kaneda, Subducted Seamount Imaged in the Rupture Zone of the 1946 Nankaido Earthquake. *Science* **289**, 104–106 (2000).

5. W. Menapace, D. Völker, N. Kaul, M. D. Tryon, A. J. Kopf, The role of mud volcanism and deep-seated dewatering processes in the Nankai Trough accretionary prism and Kumano Basin, Japan. *Geochem. Geophys. Geosystems* **18**, 2486–2509 (2017).

6. A. Noda, T. Saito, E. Fukuyama, Slip-Deficit Rate Distribution Along the Nankai Trough, Southwest Japan, With Elastic Lithosphere and Viscoelastic Asthenosphere. *J. Geophys. Res. Solid Earth* **123**, 8125–8142 (2018).

7. D. E. Byrne, D. M. Davis, L. R. Sykes, Loci and maximum size of thrust earthquakes and the mechanics of the shallow region of subduction zones. *Tectonics* **7**, 833–857 (1988).

8. J.-O. Park, T. Tsuru, S. Kodaira, P. R. Cummins, Y. Kaneda, Splay Fault Branching Along the Nankai Subduction Zone. *Science* **297**, 1157–1160 (2002).

9. A. Nakanishi, *et al.*, Detailed structural image around splay-fault branching in the Nankai subduction seismogenic zone: Results from a high-density ocean bottom seismic survey. *J. Geophys. Res.* **113**, B03105 (2008).

10. G. F. Moore, *et al.*, Three-Dimensional Splay Fault Geometry and Implications for Tsunami Generation. *Science* **318**, 1128–1131 (2007).

11. G. F. Moore, B. B. Boston, M. Strasser, M. B. Underwood, R. A. Ratliff, Evolution of tectono-sedimentary systems in the Kumano Basin, Nankai Trough forearc. *Mar. Pet. Geol.* **67**, 604–616 (2015).

12. M. Nakano, T. Hori, E. Araki, S. Kodaira, S. Ide, Shallow very-low-frequency earthquakes accompany slow slip events in the Nankai subduction zone. *Nat. Commun.* **9**, 984 (2018).

13. S. Takemura, *et al.*, A review of shallow slow earthquakes along the Nankai Trough. *Earth Planets Space* **75**, 164 (2023).

14. H. Sugioka, *et al.*, Tsunamigenic potential of the shallow subduction plate boundary inferred from slow seismic slip. *Nat. Geosci.* **5**, 414–418 (2012).

15. Y. Asano, K. Obara, T. Matsuzawa, H. Hirose, Y. Ito, Possible shallow slow slip events in Hyuga-nada, Nankai subduction zone, inferred from migration of very low frequency earthquakes. *Geophys. Res. Lett.* **42**, 331–338 (2015).

16. S. Takemura, *et al.*, Source Characteristics and Along-Strike Variations of Shallow Very Low Frequency Earthquake Swarms on the Nankai Trough Shallow Plate Boundary. *Geophys. Res. Lett.* **49**, e2022GL097979 (2022).

17. S. Takemura, K. Obara, K. Shiomi, S. Baba, Spatiotemporal Variations of Shallow Very Low Frequency Earthquake Activity Southeast Off the Kii Peninsula, Along the Nankai Trough, Japan. *J. Geophys. Res. Solid Earth* **127** (2022).

18. Y. Yamamoto, K. Ariyoshi, S. Yada, M. Nakano, T. Hori, Spatio-temporal distribution of shallow very-low-frequency earthquakes between December 2020 and January 2021 in Kumano-nada, Nankai subduction zone, detected by a permanent seafloor seismic network. *Earth Planets Space* **74**, 14 (2022).

19. T. Akuhara, Y. Yamashita, H. Sugioka, M. Shinohara, Locating tectonic tremors with uncertainty estimates: time- and amplitude-difference optimization, wave propagation-based quality control and Bayesian inversion. *Geophys. J. Int.* **235**, 2727–2742 (2023).

20. Y. Yamashita, *et al.*, Migrating tremor off southern Kyushu as evidence for slow slip of a shallow subduction interface. *Science* **348**, 676–679 (2015).

21. Y. Yamashita, M. Shinohara, T. Yamada, Shallow tectonic tremor activities in Hyuga-nada, Nankai subduction zone, based on long-term broadband ocean bottom seismic observations. *Earth Planets Space* **73**, 196 (2021).

22. K. Tamaribuchi, M. Ogiso, A. Noda, Spatiotemporal Distribution of Shallow Tremors Along the Nankai Trough, Southwest Japan, as Determined From Waveform Amplitudes and Cross-Correlations. *J. Geophys. Res. Solid Earth* **127**, e2022JB024403 (2022).

23. S. Ide, K. Imanishi, Y. Yoshida, G. C. Beroza, D. R. Shelly, Bridging the gap between seismically and geodetically detected slow earthquakes. *Geophys. Res. Lett.* **35**, 2008GL034014 (2008).

24. E. Araki, *et al.*, Recurring and triggered slow-slip events near the trench at the Nankai Trough subduction megathrust. *Science* **356**, 1157–1160 (2017).

25. X. Liu, Finite-Frequency Sensitivity Kernels for Seismic Noise Interferometry Based on Differential Time Measurements. *J. Geophys. Res. Solid Earth* **125** (2020).

26. X. Liu, G. C. Beroza, H. Li, Ambient noise differential adjoint tomography reveals fluid-bearing rocks near active faults in Los Angeles. *Nat. Commun.* (2023). https://doi.org/10.1038/s41467-023-42536-4.

27. R. B. Herrmann, C. J. Ammon, Computer programs in seismology: Surface waves, receiver functions and crustal structure. *St. Louis Univ. St Louis MO USA* (2002).

28. P. K. Miller, *et al.*, P- and S-Wave Velocities of Exhumed Metasediments From the Alaskan Subduction Zone: Implications for the In Situ Conditions Along the Megathrust. *Geophys. Res. Lett.* **48**, e2021GL094511 (2021).

29. M. W. Lee, Biot–Gassmann theory for velocities of gas hydrate-bearing sediments. *GEOPHYSICS* **67**, 1711–1719 (2002).

30. M. Nakano, *et al.*, The 2016 Mw 5.9 earthquake off the southeastern coast of Mie Prefecture as an indicator of preparatory processes of the next Nankai Trough megathrust earthquake. *Prog. Earth Planet. Sci.* **5**, 30 (2018).

31. C. Cai, D. A. Wiens, W. Shen, M. Eimer, Water input into the Mariana subduction zone estimated from ocean-bottom seismic data. *Nature* **563**, 389–392 (2018).

32. D. Bassett, D. T. Sandwell, Y. Fialko, A. B. Watts, Upper-plate controls on co-seismic slip in the 2011 magnitude 9.0 Tohoku-oki earthquake. *Nature* **531**, 92–96 (2016).

33. V. Sallarès, C. R. Ranero, Upper-plate rigidity determines depth-varying rupture behaviour of megathrust earthquakes. *Nature* **576**, 96–101 (2019).

34. G. D. Egbert, *et al.*, Fluid transport and storage in the Cascadia forearc influenced by overriding plate lithology. *Nat. Geosci.* **15**, 677–682 (2022).

35. F. Wang, *et al.*, Fluids control along-strike variations in the Alaska megathrust slip. *Earth Planet. Sci. Lett.* **633**, 118655 (2024).

36. K. M. Brown, D. M. Saffer, B. A. Bekins, Smectite diagenesis, pore-water freshening, and fluid flow at the toe of the Nankai wedge. *Earth Planet. Sci. Lett.* **194**, 97–109 (2001).

37. D. M. Saffer, Pore pressure development and progressive dewatering in underthrust sediments at the Costa Rican subduction margin: Comparison with northern Barbados and Nankai. *J. Geophys. Res. Solid Earth* **108**, 2002JB001787 (2003).

38. A. Hüpers, *et al.*, Spatiotemporal Characterization of Smectite-to-Illite Diagenesis in the Nankai Trough Accretionary Prism Revealed by Samples From 3 km Below Seafloor. *Geochem. Geophys. Geosystems* **20**, 933–951 (2019).

39. P. E. Van Keken, B. R. Hacker, E. M. Syracuse, G. A. Abers, Subduction factory: 4. Depth-dependent flux of H_2O from subducting slabs worldwide. *J. Geophys. Res.* **116**, B01401 (2011).

40. J. C. Moore, D. Saffer, Updip limit of the seismogenic zone beneath the accretionary prism of southwest Japan: An effect of diagenetic to low-grade metamorphic processes and increasing effective stress. *Geology* **29**, 183 (2001).

41. J.-O. Park, *et al.*, A low-velocity zone with weak reflectivity along the Nankai subduction zone. *Geology* **38**, 283–286 (2010).

42. T. Tonegawa, S. Takemura, S. Yabe, K. Yomogida, Fluid Migration Before and During Slow Earthquakes in the Shallow Nankai Subduction Zone. *J. Geophys. Res. Solid Earth* **127**, e2021JB023583 (2022).

43. J. Kameda, *et al.*, A new source of water in seismogenic subduction zones: A SOURCE OF WATER IN SEISMOGENIC ZONE. *Geophys. Res. Lett.* **38**, n/a-n/a (2011).

44. Y. Nishio, *et al.*, Origins of lithium in submarine mud volcano fluid in the Nankai accretionary wedge. *Earth Planet. Sci. Lett.* **414**, 144–155 (2015).

45. R. Arai, *et al.*, Upper-plate conduits linked to plate boundary that hosts slow earthquakes. *Nat. Commun.* **14**, 5101 (2023).

46. N. L. B. Bangs, *et al.*, Broad, weak regions of the Nankai Megathrust and implications for shallow coseismic slip. *Earth Planet. Sci. Lett.* **284**, 44–49 (2009).

47. W. Zhu, G. C. Beroza, PhaseNet: A Deep-Neural-Network-Based Seismic Arrival Time Picking Method. *Geophys. J. Int.* (2018). https://doi.org/10.1093/gji/ggy423.

48. L. Yang, X. Liu, G. C. Beroza, Revisiting evidence for widespread seismicity in the upper mantle under Los Angeles. *Sci. Adv.* **7**, eabf2862 (2021).

49. X. Liu, G. C. Beroza, L. Yang, W. L. Ellsworth, Ambient noise Love wave attenuation tomography for the LASSIE array across the Los Angeles basin. *Sci. Adv.* **7**, eabe1030 (2021).

50. X. Liu, G. C. Beroza, Quantifying the Effects of Nondiffuse Noise on Ballistic and Coda Wave Amplitude From Variances of Seismic Noise Interferometry in Southern California. *J. Geophys. Res. Solid Earth* **125** (2020).

51. T. M. Brocher, Empirical Relations between Elastic Wavespeeds and Density in the Earth's Crust. *Bull. Seismol. Soc. Am.* **95**, 2081–2092 (2005).

52. J. Tromp, Y. Luo, S. Hanasoge, D. Peter, Noise cross-correlation sensitivity kernels: Noise cross-correlation sensitivity kernels. *Geophys. J. Int.* **183**, 791–819 (2010).

53. A. Fichtner, Source-structure trade-offs in ambient noise correlations. *Geophys. J. Int.* **202**, 678–694 (2015).

54. J. Tromp, C. Tape, Q. Liu, Seismic tomography, adjoint methods, time reversal and banana-doughnut kernels: Seismic tomography, adjoint methods, time reversal and banana-doughnut kernels. *Geophys. J. Int.* **160**, 195–216 (2004).

55. Q. Liu, Y. J. Gu, Seismic imaging: From classical to adjoint tomography. *Tectonophysics* **566–567**, 31–66 (2012).

56. D. de Vos, H. Paulssen, A. Fichtner, Finite-frequency sensitivity kernels for two-station surface wave measurements. *Geophys. J. Int.* **194**, 1042–1049 (2013).

57. C. Tape, Q. Liu, J. Tromp, Finite-frequency tomography using adjoint methods-Methodology and examples using membrane surface waves. *Geophys. J. Int.* **168**, 1105–1129 (2007).

58. Y. O. Yuan, F. J. Simons, J. Tromp, Double-difference adjoint seismic tomography. *Geophys. J. Int.* **206**, 1599–1618 (2016).

59. G. Chen, J. Chen, C. Tape, H. Wu, P. Tong, Double-Difference Adjoint Tomography of the Crust and Uppermost Mantle Beneath Alaska. *J. Geophys. Res. Solid Earth* **128** (2023).

Abundant fluids in southern Kumano Basin linked to fluid source and slow earthquakes at plate boundary in Nankai Trough

Authors: Xin Liu[1,2], Ayako Nakanishi[1], Gou Fujie[1], Takashi Tonegawa[1], Yasuyuki Nakamura[1], Koichiro Obana[1] and Shuichi Kodaira[1]

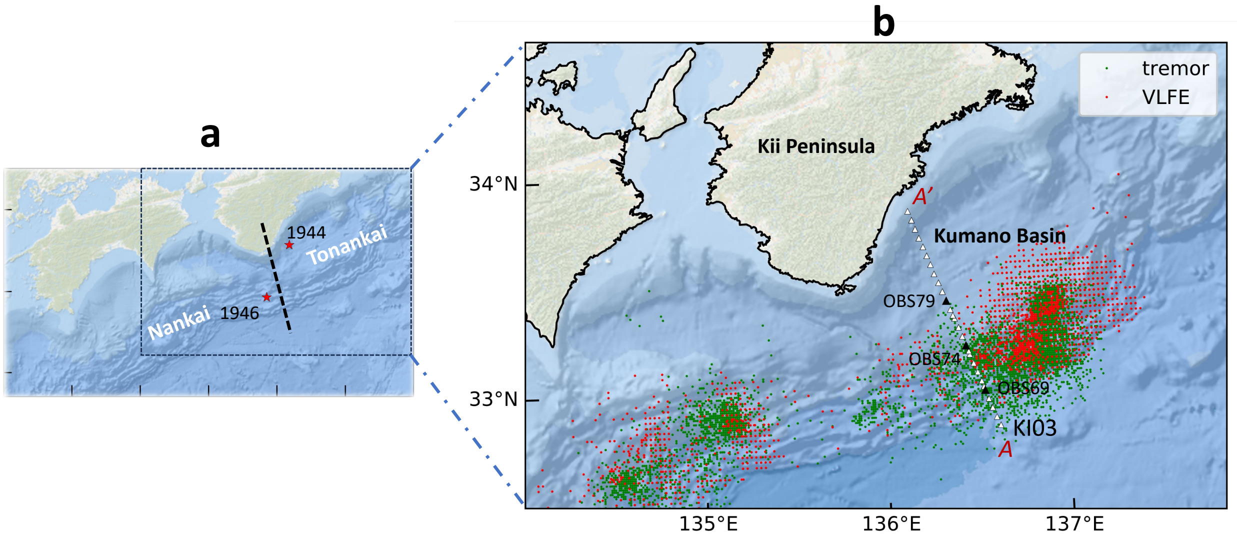

Figure 1. Map of Nankai Trough subduction zone. (a) Map with Tonankai and Nankai segments of the Nankai Trough with locations of recent megathrust earthquakes (stars). The black dashed line marks the boundary between Nankai and Tonankai regions. (b) Map of the KI03 linear OBS array off Kumano and shallow slow earthquakes. Red dots are VLFEs and green dots represent tremors. The southern Kumano Basin is between OBS74 and OBS79.

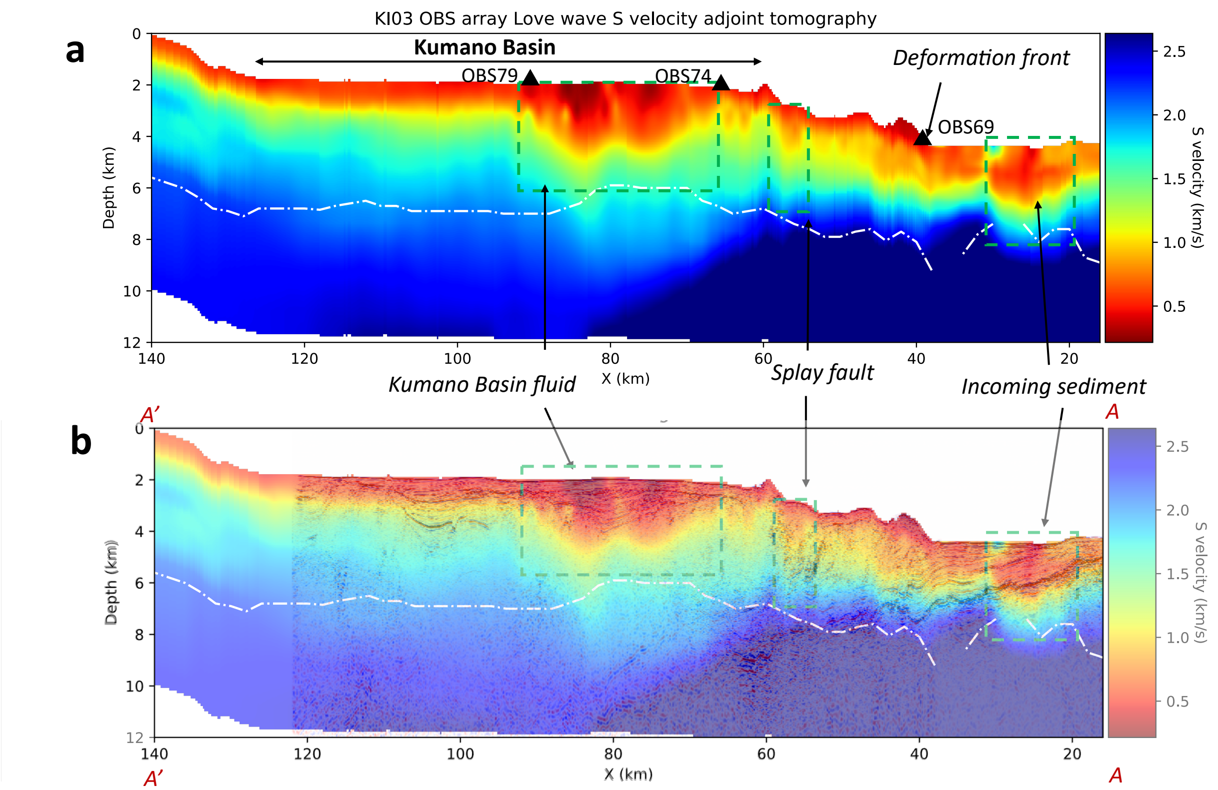

Figure 2. (a) S-wave velocity model along the KI03 array by ambient noise differential adjoint tomography. The low S velocity regions (red) are rich in fluid. (b) The same velocity model from panel a with the migrated Multi-Channel Seismic (MCS) profile overlaying on top. The seismic reflectors for Kumano Basin sediments and plate interface are clear. The white dashed line represents the depth sensitivity limit (when sensitivity drops below 10% of the peak) for Love wave at 8-s period.

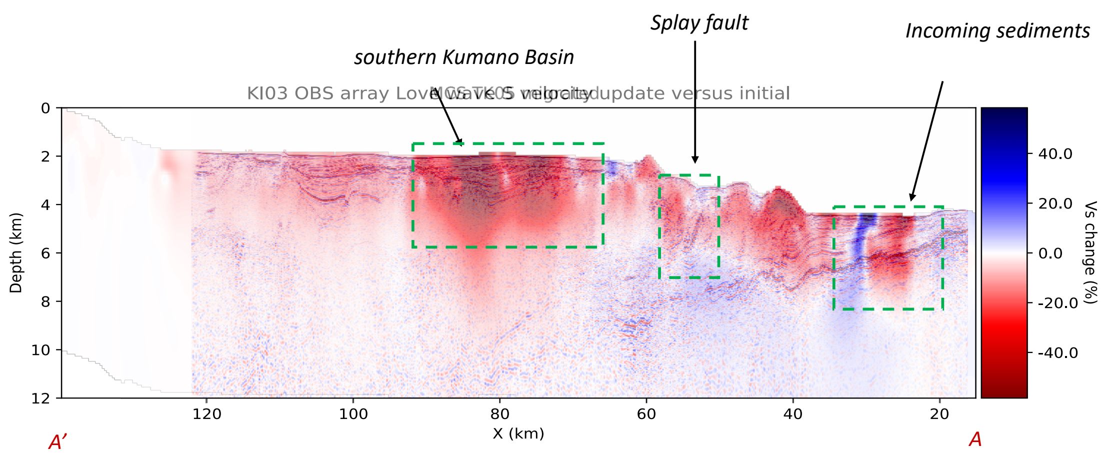

Figure 3. Adjoint tomography S-wave velocity update from initial model based on traditional ambient noise tomography. The image contains the same data as Figure 5b but is adjusted using seafloor topography. The migrated Multi-Channel Seismic (MCS) profile is overlaying on top showing the Kumano Basin sediment structure and the plate interface.

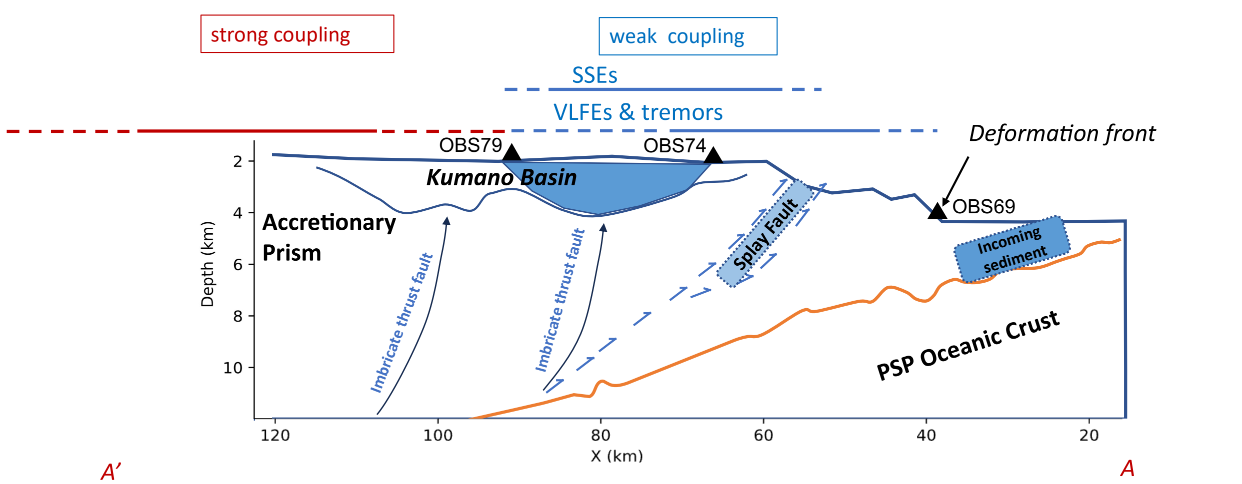

Figure 4. Cartoon of the fluid migration from plate interface to southern Kumano Basin. The blue polygons represent the fluid-rich rocks derived from adjoint tomography results, where the dark and light blue colors denote higher and lower fluid content. The imbricate thrust faults can transport fluids from plate interface to Kumano Basin. The downdip limit of slow-slip events (SSEs) is not determined.

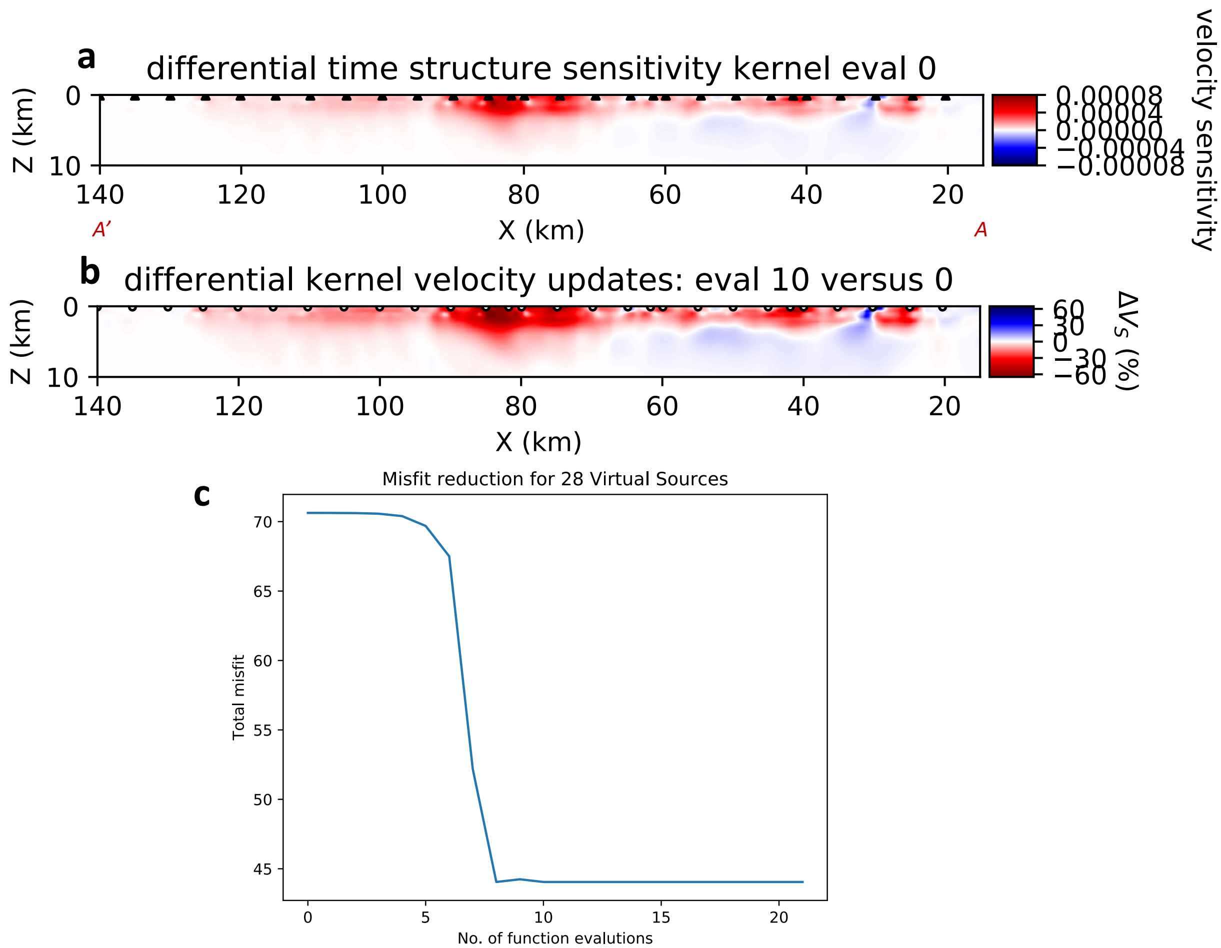

Figure 5. Iterative adjoint tomography. (a) The initial total sensitivity kernel combining all virtual sources. (b) The final shear velocity update in percentage compared to the starting model. (c) The misfit function versus iteration.